



HAL
open science

New synthesis routes and catalytic applications of ferrierite crystals. Part 2: the effect of OSDA type on zeolite properties and catalysis

Enrico Catizzone, Massimo Migliori, Tzonka Mineva, Stijn van Daele,
Valentin Valtchev, Girolamo Giordano

► **To cite this version:**

Enrico Catizzone, Massimo Migliori, Tzonka Mineva, Stijn van Daele, Valentin Valtchev, et al.. New synthesis routes and catalytic applications of ferrierite crystals. Part 2: the effect of OSDA type on zeolite properties and catalysis. *Microporous and Mesoporous Materials*, 2020, 296, pp.109988. 10.1016/j.micromeso.2019.109988 . hal-03035139

HAL Id: hal-03035139

<https://normandie-univ.hal.science/hal-03035139>

Submitted on 2 Dec 2020

HAL is a multi-disciplinary open access archive for the deposit and dissemination of scientific research documents, whether they are published or not. The documents may come from teaching and research institutions in France or abroad, or from public or private research centers.

L'archive ouverte pluridisciplinaire **HAL**, est destinée au dépôt et à la diffusion de documents scientifiques de niveau recherche, publiés ou non, émanant des établissements d'enseignement et de recherche français ou étrangers, des laboratoires publics ou privés.

1 **New synthesis routes and catalytic applications of ferrierite crystals.**

2 **Part 2: the effect of OSDA type on zeolite properties and catalysis**

3
4 *Enrico CATIZZONE^a, Massimo MIGLIORI*^b, Tzonka MINEVA^c, Stijn*
5 *van DAELE^d, Valentin VALTCHEV^e and Girolamo GIORDANO^b*

6 ^a ENEA-Italian National Agency for New Technologies, Energy and Sustainable
7 Economic Development, Trisaia Research Centre, I-75026, Rotondela (MT), Italy.

8 ^bUniversity of Calabria, Department of Environmental and Chemical Engineering, Via
9 P. Bucci – I-87036 Rende (CS), Italy.

10 ^c Matériaux Avancés pour la Catalyse et al Santé, UMR 5253 CNRS/UM/ENSCM,
11 Institut Charles Gerhardt de Montpellier (ICGM), 240, Avenue du Professeur Emile
12 Jeanbrau, 34296, Montpellier cedex 5, France.

13 ^d Total Research and Technology Feluy (TRTF), Zone Industrielle C, 7181 Feluy,
14 Belgium.

15 ^e Laboratoire Catalyse et Spectrochimie CNRS, ENSICAEN, Université de Caen Basse-
16 Normandie, 6 Boulevard Maréchal Juin, Caen, France

17
18 *Corrisponding author email : massimo.migliori@unical.it

20 **ABSTRACT**

21 *Tailoring of physicochemical properties of synthetic zeolites is of paramount*
22 *importance when these materials are applied as heterogenous catalysts. In this work,*
23 *the effect of the synthesis system and in particular of the organic structure directing*
24 *agent (OSDA) on acidity, crystal morphology, and catalytic behavior of FER-type*
25 *materials is studied. FER-type zeolites with similar Si/Al ratio and crystal size range*
26 *0.3-15 μm are synthesized by changing OSDA type or by adding surfactant. A*
27 *crystallization kinetic analysis shows that the stability of the zeolitic phase strongly*
28 *depends on the OSDA type. In particular, the crystallization time strongly affects the*
29 *purity of the FER phase when tetrahydrofuran is used as a template. Furthermore, it is*
30 *found that long amines as 1,8-diaminooctane can play a role of OSDA obtaining highly*
31 *crystalline FER-type crystals and with a high Lewis acid sites concentration. FT-IR and*
32 *^{27}Al -NMR analyses show that all of the synthesized samples possess different Lewis acid*
33 *sites concentration associated with extra-framework Al-OH species that are not*
34 *detected by NMR analysis. Catalytic tests in methanol-to-dimethyl ether reaction reveal*
35 *that synthesized samples exhibit different catalytic behavior. In particular, large (10-15*
36 *μm) FER-type catalyst synthesized with tetrahydrofuran suffer deactivation caused by a*
37 *higher carbon deposit level. On the contrary, nano-sized FER-type crystals, prepared*
38 *by using pyrrolidine as OSDA and a surfactant, exhibits high selectivity and*
39 *considerable resistance to coke deposition.*

40

41 **Keywords:** Ferrierite zeolite, synthesis, crystal morphology, Brønsted-Lewis acidity,
42 methanol conversion.

43 1. INTRODUCTION

44 Activity, selectivity and stability of zeolites catalysts are recognised to depend upon
45 several factors as zeolite structure, crystal size and nature of active sites. Zeolite channel
46 system (channel orientation and opening size) and diffusion pathway are well-known
47 factors affecting the accessibility of the active sites, products distribution and catalyst
48 deactivation [1-5] strongly. Zeolites channel system is also a critical factor that controls
49 the deactivation by coke deposition; thus zeolites with lower channels dimensionality
50 suffer from more rapid deactivation [6].

51 Nevertheless, zeolites with a similar channel system can exhibit different catalytic
52 behaviour depending on the nature of acid sites. Hence, the acid sites concentration,
53 typology (Brønsted and Lewis), strength, and location are important parameters when
54 zeolites are applied as heterogeneous catalysts [7-13].

55 Furthermore, catalyst resistance to deactivation as well as catalyst effectiveness can be
56 improved by changing the size and morphology of zeolite crystals [14-16]. In particular,
57 the application of nano-sized or hierarchical zeolite crystals permits to reduce coke
58 formation and enhance the diffusion of reactant species improving catalyst
59 performances [17-19].

60 Therefore, the ability of zeolite to be modified by both *in situ* and post-synthesis
61 treatments is of considerable importance for the industrial perspective, particularly in
62 the area of heterogeneous catalysis [20-23].

63 Ferrierite (FER) is an important zeolite applied in applied as catalyst in the skeletal
64 isomerization of n-butene for the production of iso-butene and as additive to ZSM-5
65 catalyst in the dewaxing by selective cracking process for the production of lubricant

66 [24]. FER framework consists of an intersecting 2-dimensional system of 10- (5.4 x 4.2
67 Å) and 8- (4.8 x 3.5 Å) member ring channels and can be synthesised with Si/Al ratios
68 ranging from 5 to infinity [25, 26]. The particular channel configuration of FER
69 framework is appropriate for processing small molecules. In particular, FER-type
70 crystals have recently ranked as a reliable acid catalyst for dimethyl ether (DME)
71 production. DME is considered a reliable alternative fuel for Diesel engines thanks to
72 its high cetane number, low ignition-temperature and soot-free exhausted gases [27-31].
73 Furthermore, DME is an essential intermediate compound in olefins production from
74 methanol [32, 33]. DME can be produced by either double-step or one-step route [31].
75 Briefly, in the double-step process, methanol is synthesised from syngas over copper-
76 based catalysts, purified and then dehydrated to DME in a separate reactor over an acid
77 catalyst. In one-step process, both synthesis and dehydration of methanol are carried out
78 in a single reactor over a multi-functional metal/acid catalyst. From an economic point
79 of view, one-step process seems to be more profitable. Furthermore, a growing attention
80 is receiving the one-step DME synthesis starting from CO₂-rich syngas or CO₂/H₂
81 mixture [34]. γ -Al₂O₃ is the most studied catalyst for the methanol dehydration step
82 thanks to the high selectivity towards DME at the typical reaction temperature adopted
83 for both the direct and the indirect routes, inhibiting olefins formation thanks to its low
84 acidity [31]. Although this indisputable advantage, high reaction temperature is
85 necessary (about 300 °C) to promote satisfactory results in terms of methanol
86 conversion. Furthermore, the presence of water molecules formed during the reaction
87 suppress the activity of Lewis acid sites of γ -Al₂O₃ [34, 35]. Moreover, low DME
88 productivity is obtained during one-pot CO₂-hydrogenation over CuZn/ γ -Al₂O₃, where
89 a lot amount of water is formed and low temperature are requested for a thermodynamic

90 point of view [36-38]. For these reasons, research is focusing on the development of
91 new catalysts with high activity at relatively lower temperature as well as high stability
92 in presence of water. Zeolites are investigating as alternative acid catalysts to γ -Al₂O₃,
93 although physicochemical properties shall be carefully selected. In fact, as reported in
94 recent works, channel system, acidity and crystal morphology of zeolites strongly affect
95 the catalytic behaviour in terms of DME yield, deactivation and coke formation [39-43].
96 For instance, during methanol dehydration reaction, high coke deposition rate is found
97 for zeolites with 3-dimensional channel system such as MFI, BEA or CHA, while fast
98 deactivation is observed for zeolite with 1-dimensional channel system such as TON,
99 MTW and EUO [39, 41]. On the contrary, FER-type catalyst exhibits high resistance to
100 deactivation and a high inhibiting-features toward coke formation during methanol
101 dehydration reaction. The superiority of FER over the other investigated zeolites was
102 related to its 2-dimensinal channel system with small/medium pore openings that ensure
103 high shape-selectivity towards DME [39]. Moreover, the superiority of FER-type
104 zeolite over γ -Al₂O₃ in terms of resistance in presence of water was recently reported
105 [40].

106 The utilization of zeolites as acid catalysts for one-pot CO₂/CO hydrogenation was also
107 assessed. The physicochemical properties of zeolites strongly affect the catalytic
108 behaviour of multifunctional catalyst. Even the preparation method of the
109 multifunctional catalyst is of paramount importance. For instance, a superior catalytic
110 performance was demonstrated on hybrid catalysts prepared by oxalate co-precipitation
111 of copper, zinc and zirconium over zeolite crystals respect to conventional mechanical
112 mixture. The generation both of metal-oxides and acid sites in a single grain leads to an
113 increased CO₂ conversion. In particular, when FER-type zeolite is used as dehydration

114 component, higher DME productivity is obtained respect to other zeolites, i.e. MFI and
115 MOR. CuZnZr-FER hybrid catalyst offers a promising DME production via CO₂
116 hydrogenation process thanks to more efficient redox-acid cooperation to convert CO₂
117 into methanol and dehydrate rapidly the alcohol into DME with low production of by-
118 products as carbon monoxide [44-47]. The superiority of FER over other zeolite
119 structures (i.e. TON, MFI, MOR, MTT, FAU) in the syngas-to-DME process was also
120 pointed out by several studies [48-54]. All of this results indicate that the careful choice
121 of the properties of acid catalyst is fundamental for DME production via both tow-step
122 (methanol dehydration) or one-step (syngas/CO₂-to-DME) synthesis way.

123 As extensively reported, the physicochemical properties of zeolites are highly
124 dependent on the synthesis procedure adopted for the synthesis. For instance, the choice
125 of organic structure directing agent (OSDA) is of paramount importance for aluminium
126 distribution, acidic properties and crystals size, being these key parameters for catalysis
127 [55, 56].

128 The present study is devoted to the fine control of the physicochemical properties of
129 FER-type catalysts. The series of samples were synthesised by adopting different
130 synthesis conditions in order to obtain crystals with different acid sites distribution and
131 morphology. Pyrrolidine, ethylenediammine, 1,8-diaminooctane and tetrahydrofuran
132 were used as OSDA. Furthermore, a small addition of sodium lauryl sulphate to the
133 synthesis gel permits to reduce crystal size with no effect on crystallinity.

134 Brønsted/Lewis acid sites distribution and concentration of synthesised materials have
135 been investigated with NH₃-TPD and FT-IR of adsorbed D₃-acetonitrile while crystals
136 morphology has been analysed by scanning electron microscopy. Methanol dehydration
137 to dimethyl ether catalytic tests in the reaction temperature range 180-240 °C, has

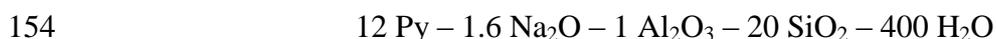
138 permitted to evaluate the catalysts in terms of activity, selectivity, deactivation, and
139 coke formation. The set of experimental data can be used to tailor the properties of
140 FER-type catalysts.

141 **2. EXPERIMENTAL**

142 *2.1 Samples preparation*

143 Four different OSDA: pyrrolidine (Py), ethylenediamine (En), tetrahydrofuran (THF)
144 and 1,8-diaminooctane (DAO) were used to synthesise FER samples from a synthesis
145 gel with a Si/Al ratio in the range 8-10. The following chemicals were used in all the
146 synthesis: colloidal silica Ludox AS-40 (SiO₂, 40 wt% suspension in H₂O, Aldrich),
147 sodium aluminate (NaAlO₂, Aldrich), aluminium sulphate (Al₂(SO₄)₃·16H₂O, Aldrich),
148 sodium hydroxide (pellets, Aldrich), pyrrolidine (Aldrich) ethylenediamine (Fluka),
149 tetrahydrofuran (Aldrich), 1,8-diaminooctane (Aldrich), sodium lauryl sulphate
150 (Aldrich) and distilled water. Synthesis gels were prepared at room temperature, and the
151 crystallization was carried out in stainless-steel Teflon coated autoclave.

152 Synthesis of FER sample by using pyrrolidine (Py-FER) as OSDA was prepared by
153 adopting the following synthesis gel molar composition [33]:



155 In a typical synthesis, sodium aluminate, NaOH and pyrrolidine were dissolved in
156 distilled water and the mixture was stirred until complete dissolution of components.
157 Afterwards, colloidal silica was added dropwise to the solution, and the gel was stirred
158 for 1 hour. The obtained gel transferred in an 80 mL autoclave and left for 30-90 hours
159 at 180 °C in a tumbling oven (rotation speed: 15 rpm).

160 The effect of a surfactant on crystal morphology of the Py-FER, was evaluated by
161 adding sodium lauryl sulphate (SLS) with an SLS/Al₂ molar ratio equals to 0.3 at the
162 above described synthesis gel, and the obtained sample is labelled as SLS-Py-FER.

163 Synthesis of FER sample by using ethylenediamine (En-FER) was carried out by
164 adopting the following synthesis gel molar composition [33]:



166 Sodium aluminate, NaOH and ethylenediamine were dissolved in distilled, and the
167 mixture was stirred until complete dissolution of components. Afterwards, colloidal
168 silica was added dropwise to the solution, and the gel was stirred for 1 hour. The
169 obtained gel transferred in a 120 mL autoclave and left for 3-12 days in the same
170 conditions of the Py-FER synthesis.

171 The synthesis of FER sample by using 1,8-diaminooctane as OSDA was performed by a
172 replacing ethylenediamine as it follows:



174 NaOH and sodium aluminate were dissolved in distilled water and the mixture was
175 stirred until complete dissolution of components. Afterwards, a DAO in water solution
176 was added and the resulting phase was mixed for 30 minutes. Finally, colloidal silica
177 was added dropwise and the obtained gel was stirred for 1 h prior to transfer it in an
178 autoclave with a volume of 60 mL. Crystallization was performed by adopting the same
179 procedure described for En-FER. More details are reported elsewhere [ref].

180 The synthesis of FER sample with tetrahydrofuran as OSDA (THF-FER) was
181 performed by adopting the procedure published by Guo et al. [55] with the following
182 synthesis gel molar composition:

183 $10 \text{ THF} - 4.3 \text{ Na}_2\text{O} - 20 \text{ SiO}_2 - 1 \text{ Al}_2\text{O}_3 - 400 \text{ H}_2\text{O}$
184 NaOH aqueous solution was added dropwise to a mixture of aluminium sulphate
185 colloidal silica and water. The obtained phase was stirred for 1 h and tetrahydrofuran
186 was added under vigorous stirring. After 1 h, the gel was transferred in an autoclave
187 with a volume of 60 mL and kept at 200 °C for 6-12 days in a static oven [55].
188 After crystallization, the solid was separated by vacuum filtration and washed several
189 times with distilled water until the pH of filtered solution was close to the neutral value.
190 The obtained white solid was then dried for 15 hours in a static oven kept at 80 °C. In
191 order to remove template from zeolite, air-flow calcination was carried out at 550 °C
192 with an holding time of 8 hours and a heating rate of 2 °C/min. Afterwards, H-form
193 solid was obtained by ion-exchange with a NH₄Cl 1 M solution at 80 °C followed by a
194 secondary air-flow calcination under the same condition of the previous one [56].

195

196 *2.2 Physicochemical characterization*

197 X-Ray powder diffraction (APD 2000 Pro) (region $5^\circ < 2\theta < 50^\circ$, step 0.02°/ s) was
198 used to verify both purity and crystallinity of obtained phase; the morphology of the
199 crystalline phase was observed on a scanning electron microscope (SEM, FEI model
200 Inspect) and a transmission electron microscopy (TEM, Philips CM12). Atomic
201 absorption spectroscopy (ContraAA® 700 – Analytik Jena) was used for the
202 measurement of content of sodium, aluminum and silicon content in the calcined
203 catalysts.

204 The specific surface area (by B.E.T. method) and the micropores volume (by *t*-plot
205 method) of the calcined samples were obtained by nitrogen adsorption/desorption
206 isotherms at -196 °C with a ASAP 2020 instrument (Micromeritics).

207 The ^{27}Al -NMR spectra were acquired on a Bruker Advance 500 MHz instrument at
208 130.3 MHz with radiofrequency power of 54 kHz, a pulse length of 4.6 μs with a
209 corresponding angle theta of $\pi/4$. Rotors were spun at 14 kHz, and the recycle delay
210 used for both nuclei was 1 second.

211 Surface acidity of H-form sample was measured by both NH_3 -TPD analysis
212 (TPDRO1100, ThermoFisher) and FT-IR analysis by using D_3 -acetonitrile as a probe
213 molecule. Detailed procedure is reported elsewhere [57].

214

215 *2.3 Catalytic tests*

216 Catalytic tests were performed in the temperature range 180 – 240 $^\circ\text{C}$ using an
217 experimental apparatus described elsewhere [59, 65]. A mixture of methanol (0.06
218 mol/mol) and nitrogen as a carrier (60 Nml min^{-1}) was fed in a quartz reactor loaded
219 with 70 mg of catalyst in pellets form (300 – 500 μm) fixing the Weight Hourly Space
220 Velocity (WHSV) at $4.5 \text{ g}_{\text{MeOH}} \cdot (\text{g}_{\text{cat}} \cdot \text{h})^{-1}$. Prior to any test, the catalyst drying was
221 performed under nitrogen flow at 240°C for 3 h.

222 The product stream composition was determined by a gas chromatograph (Agilent
223 7890A), equipped with a capillary column (J&W 125–1032) and an FID detector.

224 Catalyst resistance against deactivation was investigated in Time-On-Stream (TOS)
225 measurements carried out at 240 $^\circ\text{C}$ for about 1000 min. The amount of retained
226 carbonaceous species deposited during TOS test was measured by thermo-gravimetric
227 analysis (TGA) in air flow by heating the sample from room temperature to 850 $^\circ\text{C}$
228 (heating rate $5 \text{ }^\circ\text{C} \cdot \text{min}^{-1}$) and attributing the sample weight loss observed between 250
229 and 700 $^\circ\text{C}$ to the deposited carbonaceous species [58].

230 **3. RESULTS AND DISCUSSION**

231 *3.1 Structural properties of FER-type zeolites synthesized with different OSDA*

232 X-ray patterns as a function of crystallization time of En-FER, Py-FER, and THF-FER
233 are reported in Figure 1A-C. Crystal growth kinetics of En-FER is relatively slow (see
234 Figure 1A) as traces of FER phase are observed after 3 days and after 6 days the
235 crystalline phase is dominant. A crystallization time of 10 days can be considered as
236 optimal to obtain high crystalline En-FER since, for longer time (12 days), traces of
237 kaetite phase appear. A faster crystal growth kinetic is observed for the system
238 containing pyrrolidine (Py-FER) (see Figure 1B). Although no crystalline phases were
239 observed after 15 hours, the onset of FER-phase crystallization is evident after 30 hours
240 and is completed in the range 60-90 hours. The obtained results are in good agreement
241 with Chen et al. [33], except for some minor differences in terms of crystallization time
242 values that usually arise when different autoclaves volumes are adopted. Furthermore,
243 the addition of sodium lauryl sulphate (SLS-Py-FER) does not affect crystallinity as can
244 be seen in Figure S.1.

245 *Nevertheless, some differences may be noted after 15 h crystallization. In fact, SLS-Py-*
246 *FER seems to have a higher crystallinity than Py-FER. The presence of surfactant may*
247 *be responsible of formation of microdroplets that mimic crystallization favouring*
248 *nucleation [59]. The higher nucleation rate may be responsible of the formation of*
249 *smaller crystals in SLS-Py-FER sample as later reported.*

250 Guo et al. [55] showed that, for a THF-containing system, crystallization of FER phase
251 occurs in time range 8-12 days, without mentioning any information about the
252 crystallinity evolution over time. Therefore, the crystal growth kinetics of THF-FER
253 was studied and the results are presented in Figure 1C. XRD results show that the THF-
254 containing system yields FER-type phase, but the crystallization time is a key parameter

255 to be properly chosen, in order to maximise the phase purity. In fact, after 6 days, FER
256 X-Ray peaks appear still with a significant amount of amorphous phase and
257 crystallization time of 8 days can be suggested as optimal value to obtain high
258 crystalline and pure ferrierite (THF-FER sample). Longer crystallization time causes the
259 formation of competitive phases such as MOR and MFI. The formation of MOR phase
260 in this system can be attributed to the higher sodium concentration in the THF-
261 containing synthesis gel (Na/Al=4.3 mol/mol) higher than the previous investigated
262 systems (En-FER, Na/Al=1.85; Py-FER, Na/Al=1.6).

263 The replacing of En with DAO reduce the induction period as reported in Figure 1-D In
264 fact, in presence of DAO, FER-phase is almost completely crystallized after 3 days
265 whilst only traces of crystalline product is observed when ethylenediamine is used as
266 OSDA.

267 Figure 2 shows representative SEM micrographs revealing that all samples exhibit the
268 typical of ferrierite plat-like morphology with a well-developed $\{1\ 0\ 0\}$. However, the
269 crystals differ in size and the level of agglomeration. The En-FER crystals (Figure 2A)
270 have the following characteristics: length 2-3 μm , length/width ratio around 2 and
271 thickness 100 nm, while DAO as OSDA generates smaller crystals with size around 1
272 μm and lower length/width ratio (around 1.3) as reported in Figure 6D. Py-FER sample
273 shows larger crystals with length 5-6 μm , length/width ratio around 1.6 and thickness
274 100 nm (Figure 2B). Completely different crystal morphology was observed for THF-
275 FER sample (Figure 2C) where uniform agglomerates of 10-15 μm are observed, as
276 each agglomerate consists of stacked plat-like crystals with thickness around 150 nm.
277 For THF-containing system, it should be reminded that the crystallization is relatively
278 long and the XRD study reveals the presence of other solids (Figure 1.C). Accordingly,

279 SEM micrographs after 6 and 12 days of crystallization, reported in Figure S.2, confirm
280 the presence of an amorphous phase after 6 days, whilst MFI and MOR phases are
281 clearly present after 12 days. The attribution of crystals to MFI rather MOR phases was
282 carried out referring to SEM analysis reported by Qian et al. [60].

283 SEM and TEM pictures of SLS-Py-FER sample are reported in Figure 3. They are
284 significantly smaller than the sample synthesised without sodium lauryl sulphate (Figure
285 6B). The morphology is plate-like and the size below 500 nm. Thus the addition of the
286 surfactant inhibits the growth of the crystals, but retains the high crystallinity of the
287 zeolite (*vide supra*).

288 The results of N₂ adsorption analysis are summarized in Table 1. Micropore volume
289 follows the order THF-FER < DAO-FER < Py-FER ≈ SLS-Py-FER < En-FER. The lower
290 micropore volume values observed for THF-FER and DAO-FER can be related to the
291 higher amount of sodium cations in zeolite channels. Figure S.3 (Supporting
292 Information) highlights the adsorption/desorption isotherms of synthesised samples in
293 protonic form. All of the investigated structures exhibit the pattern of type I isotherm
294 typical of microporous materials [33].

295 Figure 2 shows the ²⁷Al MAS NMR spectra of the H-form FER-type zeolites obtained
296 in En-, Py-, DAO- and THF-containing systems. They are dominated by a signal
297 centered at around 55 ppm, characteristic of tetra-coordinated aluminium species in
298 zeolite framework. The presence of a second peak at around 62 ppm for Py-FER sample
299 can be associated with tetrahedral aluminium species with a different Al-O-Si bond
300 angle [68]. A relatively weak signal at around 0 ppm revealing the presence of
301 octahedral extra-framework aluminium (below 10%). The observed quadrupolar line

302 broadening can be caused by distortions of the octahedral symmetry of AlO_6 sites. No
303 octahedral aluminium species were observed on THF-FER sample by NMR analysis.

304 It is well-known that the zeolite structure is generated by a network of SiO_4 and AlO_4^-
305 tetrahedral linked together by a shared oxygen atom. Due to the presence of trivalent
306 atoms (e.g. aluminium) in the tetrahedral units, the framework offers a negative charge
307 which needs to be balanced with non-framework exchangeable cations that are
308 generally elements of the group IA and group IIA as sodium, potassium, magnesium
309 and calcium [69]. In this work, sodium is used to synthesise FER-type materials, and
310 this is the cation that balances negative charges associated with aluminium atoms.
311 Furthermore, the high quantity of tetrahedral aluminium species detected by NMR
312 analysis, suggests that the Na/Al ratio should be around one. Strikingly, the chemical
313 analysis reported in Table 1 shows that Na/Al is about 0.10 for Py-FER and En-FER,
314 0.6 for DAO-FER and 0.9 for THF-FER. These results disagree with the previous
315 theoretical assumption, suggesting that sodium cations do not balance an important
316 amount of aluminium species in tetrahedral position. Vuono et al. [67] reported a Na/Al
317 ratio value below to unity (around 0.60) for MCM-49 materials synthesised in the
318 presence of hexamethylenimine despite aluminium was mainly tetra-coordinated as in
319 our case. Forbes et al. [71, 72] report that during the synthesis of ZSM-5/Theta-1
320 materials in the presence of diethanolamine, the organic molecules were considered to
321 have both a pore-filling role and charge compensatory role. Furthermore, Rollmann et
322 al. [73] assert that protonated amine (e.g. ethylamine, pyrrolidine, hexamethylenimine)
323 play the role as counterion of negative charge associated to tetrahedral aluminium atoms
324 located into zeolite framework, also for FER-type materials. Therefore, because in this
325 work, aluminium atoms are mainly present in tetrahedral coordination, protonated

326 organic molecules can be reasonably present to compensate negative charge of zeolite
327 lattice. THF-FER exhibits a relative higher Na/Al ratio (around 0.9) showing that AlO_4^-
328 species needs to the presence of sodium cations to be balanced because THF is not able
329 to play a role of counterion [74]. Nevertheless, also for THF-FER, the Na/Al ratio is not
330 equal to one, suggesting the presence of extra-framework aluminium species not
331 detected by the NMR analysis. This aspect will be elucidated during FT-IR results
332 discussion.

333

334 *3.2 Zeolite acidity*

335 The NH_3 -TPD profiles are reported in Figure 9 for all the synthesised samples
336 displaying three main peaks characterised by different ammonia maximum desorption
337 temperatures peaks (T_M) as an indicator of different acid sites family (the higher is T_M ,
338 the stronger is the acid sites). No differences in NH_3 -TPD profiles can be observed
339 between Py- and SLS-Py-FER (see Figure S. 4), indicating that the presence of
340 surfactant affects crystal morphology rather than acid properties.

341 As suggested by Niwa and Katada [76, 77], the interpretation of peaks with $T_M < 300$ °C
342 may be quite misleading since the desorption effect may also be related to physically
343 adsorbed ammonia interacting via a hydrogen bond with the NH_4^+ ions adsorbed onto
344 acid sites. In this condition, having comparable desorption energy, the presence of weak
345 acid sites, may be partially hidden by physisorbed ammonia. On the contrary, the peaks
346 with $300^\circ\text{C} < T_M < 500$ °C are associated with ammonia molecules desorbed from strong
347 acid sites (both Brønsted and Lewis acid sites). The peak with $T_M > 700$ °C can be
348 associated to dehydroxylation phenomena [78, 79] since it is detected either in NH_3 -

349 TPD experiments or in the corresponding “blank” TPD experiments performed over the
350 same catalyst and under the same experimental conditions, without NH₃ feed (see
351 Figure S.5 of supplementary information). Weight loss above 700 °C was also detected
352 via TG analysis (Figure S. 6 for THF-FER) for the protonic form of the sample
353 revealing that the dTG peak above 700°C as a dehydroxylation phenomena.

354 Quantitative results of NH₃-TPD measurements reported in Table 2 indicates how the
355 total acid sites concentration follows the Si/Al ratio on the solid.

356 Figure 10 depicts the FT-IR spectra of H-ferrierite samples in the OH-stretching region.
357 Two main bands observed at 3745 cm⁻¹ and 3600 cm⁻¹ are associated with terminal
358 silanol Si-OH and Brønsted acid sites Al-OH-Si groups, respectively [80, 81]. A
359 shoulder at around 3645 cm⁻¹ is also present. Similar result was reported already [34,
360 82], but the peak is not well-identified. Peixoto et al. [83] suppose that the observed
361 shoulder can be associated to a silanol group anchored on extra-framework aluminium
362 species (e.g., octahedral aluminium) as reported also by Rachwalik et al. [84] even
363 though in the investigated samples, NMR analysis suggests that octahedral aluminium
364 species are nearly absent. It is known from the literature that aluminium in highly
365 distorted coordination might become NMR silent and the observed band at 3645 cm⁻¹
366 can be associated to OH groups connected to the so called ‘invisible’ aluminium species
367 [85, 86] that can play a role of Lewis acid sites [87, 88]. The presence of these species
368 could explain the non-stoichiometric Na/Al ratio discussed above.

369 Curves of Figure 10 indicate that THF-FER sample seems to possess a lower
370 concentration of both terminal silanol Si-OH and Al-OH groups compared with the
371 other samples. Figure S.7 (Supporting Information) reveals that PY-FER and SLS-PY-

372 FER samples exhibit similar FT-IR spectra in the OH-stretching region except for a
373 slightly lower Si-OH concentration for the surfactant-free sample.

374 In order to discriminate between Lewis and Brønsted acid sites, deuterated acetonitrile
375 (CD_3CN) was used as a probe molecule following the FT-IR procedure discussed
376 above. FT-IR spectra of adsorbed CD_3CN at different desorption temperatures (ranging
377 between 25°C and 300°C) are reported in Figure 11. The presence of two main bands at
378 about 2296 cm^{-1} and 2322 cm^{-1} reveals the presence of both Brønsted and Lewis acid
379 sites, respectively, in all catalysts. Smaller bands at lower wave length associated with
380 physisorbed acetonitrile are also presents [64]. The concentration of Brønsted and
381 Lewis sites were obtained from the integral intensities of the IR bands of adsorbed
382 CD_3CN at 2296 cm^{-1} and 2322 cm^{-1} , respectively, by using the extinction factor
383 coefficients reported in Section 2. Brønsted and Lewis site distribution of the
384 investigated samples was calculated from the area of bands recorded at 25°C , and
385 quantitative results in terms of Lewis acid site percentage are summarized in Table 2.
386 Results show that OSDA significantly effects acid sites distribution: the En-FER and
387 DAO-FER exhibit a high Lewis acid sites concentration (around 40%) while the lowest
388 value was 15% of THF-FER. The addition of surfactant did not affect the acid sites
389 distribution as both Py-FER and SLS-Py-FER samples exhibit the same concentration
390 of Lewis acid sites (around 33%). Therefore, considering NH_3 -TPD profiles, it is
391 possible to conclude that Py-FER and SLS-Py-FER have a very similar acidity in terms
392 of concentration, distribution, and typology of acid sites, but substantially different
393 crystal size.

394 In order to estimate the number and the strength of Brønsted and Lewis acid sites the
395 desorption profiles shown in Figure S. 8 were analyzed and the results are reported in

396 Figure 11. The set of data show that Lewis acid sites are stronger than Brønsted ones for
397 all the samples. The desorption of Brønsted sites becomes significant above 150°C
398 while the Lewis sites are still occupied above 300°C. Only EN-FER sample seems to
399 exhibit slightly weak Lewis acid sites since the desorption of probed molecule starts at a
400 lower temperature. On the contrary, for Brønsted acid sites the acetonitrile molecules
401 desorption starts from 50°C and no occupied sites are present above 250°C. EN-FER,
402 PY-FER and DAO-FER exhibit a similar trend, whilst THF-FER had Brønsted acid
403 sites weaker than the other catalysts. In fact, at 100 °C the 60% of the Brønsted acid
404 sites are desorbed for THF-FER compared with 30% for the other samples.

405 By considering as strong Lewis acid sites fraction, the value of Lewis acid sites still
406 occupied by CD₃CN molecules at 300 °C, it is possible to calculate the the fraction of
407 Strong Lewis sites reported in (Table 2, last column). The concentration of strong Lewis
408 acid sites follows the order DAO-FER>En-FER>Py-FER (≈SLS-Py-FER)>THF-FER
409 suggesting that synthesis system affect both typology and strength of acid sites. The
410 observed Lewis acid sites can be associated with extra-framework, NMR silent, Al-OH
411 species.

412 *3.4 Catalytic tests*

413 The catalytic activity of synthesised samples was investigated by performing Methanol
414 to dimethyl ether reaction. Figure 13 shows the methanol conversion at different
415 reaction temperatures. The data were calculated as an arithmetic media over three
416 independent measurements during 30 min of Time-On-Stream, always resulting in
417 conversion relative variation below 10%.

418 The catalytic data show that differences in textural and chemical properties lead to
419 different catalytic activity, except for THF-FER, exhibiting the lowest value of
420 methanol conversion on the investigated reaction conditions. Significant differences in
421 conversion between the samples, excluding THF-FER, which shows substantially lower
422 activity, can be found only at a temperature below 200°C. The lower activity of THF-
423 FER is attributed to the large crystal size, increasing the mass transfer limitation. The
424 effect of crystal size is also evident by comparing Py-FER and SLS-Py-FER that exhibit
425 similar acidity (acid sites concentration and distribution) but different activity. At the
426 reaction temperature of 180°C, methanol conversion on Py-FER is 15% lower than on
427 SLS-Py-FER but the effect tends to disappear when increasing the temperature. DME
428 selectivity data reported in Figure 14 suggest that over both THF-FER and DAO-FER
429 sample only DME is formed at 180 °C whilst a slightly lower selectivity is observed
430 over the others sample. For all the samples, DME selectivity progressively decreases as
431 the reaction temperature increases, and methane, ethylene, propylene and butenes
432 appear in the reaction products.

433 In order to assess the catalyst stability, the methanol conversion was monitored for
434 about 1000 minutes at 240°C (Figure 15). FER-type catalysts synthesised employing
435 amines as OSDA (En-FER, Py-FER, and DAO-FER), offer high stability in the
436 considered time range. On the contrary, THF-FER shows a progressive deactivation
437 with a conversion drop of about 10% at the end of the test.

438 The higher deactivation rate observed for THF-FER sample can be attributed to the
439 amount of deposited coke, significantly higher for this sample, as reported in Figure 16.
440 The higher carbon deposit level and the consequent rapid deactivation can be promoted
441 by both largest presences of Brønsted acid sites or by bigger crystal size as both

442 characteristics are present in THF-FER sample. On the contrary, despite the similar
443 acidic properties, the carbon deposit level exhibited by SLS-Py-FER lower than Py-FER
444 can be attributed to nano-sized crystals retarding coke formation [92, 93]. In this
445 direction also goes DAO-FER sample showing a carbon deposit lower than the others
446 micro-sized samples, despite its higher acid sites concentration.

447

448 **4. CONCLUSIONS**

449 FER-type crystals were synthesized employing pyrrolidine (Py) ethylenediamine (En),
450 tetrahydrofuran (THF) as OSDA with the goal to vary the chemical, physical and
451 textural properties of the zeolite. For the first time, 1,8-diaminooctane (DAO) was used
452 as OSDA, and its role in the formation of FER-type structure was studied combining
453 experimental and theoretical methods. A surfactant (sodium lauryl sulphate - SLS) was
454 used in order to tune the crystal size of Py-FER and thus nano-sized crystals were
455 synthesized. SLS-obtained nanosized crystals showed similar acidity and improved
456 catalytic activity with respect to the micron-sized Py-FER counterpart. Differences in
457 crystal size and morphology were also found when changing the OSDA, from very
458 large crystals in the case of THF-FER to a typical morphology of ferrierite obtained
459 with amino-containing OSDA. Despite similar Si/Al ratios of the initial gels the use of
460 different organic structure directing agents leads to variation of the zeolite framework
461 composition. The OSDA impacts on the Al distribution resulting in catalysts with
462 significant differences in acid sites distribution and strength (Lewis and Brønsted). This
463 result provides new opportunities in tailoring the acid characteristics of FER-type
464 catalysts. This statement is fully supported by the results obtained in the methanol
465 dehydration to DME. Both acidity and crystal size strongly affect the DME selectivity

466 and resistance towards deactivation. A higher coke amount is deposited on bigger
467 crystals, whilst the utilization of nano-sized crystals strongly retard coke formation. In
468 the light of acidity analysis, one can state that the higher is Lewis acid sites
469 concentration the better performing is the catalyst for DME production. On the other
470 side the large presence of Brønsted acidity seems to promote the abundant coke
471 formation.

472

473 **ACKNOWLEDGMENTS**

474 The authors gratefully acknowledge dr. Eddy Dib, Catalysis and Spectroscopy
475 Laboratory LCS ENSICAEN, for NMR analysis and dr. Francesco FRUSTERI, CNR-
476 ITAE “Nicola Giordano” - Messina, for TEM micrographs.

477

478 **REFERENCES**

- 479 [1] J. Čeika, A. Krejčí, N. Žilková, J. Kitrla, S. Ernst, A. Weber, *Microp. Mesopor.*
480 *Mater.* 53 (2002) 121-133.
- 481 [2] B. J. Schoeman, E. Babouchkina, S. Mintova, V. P. Valtchev, J. Sterte, J.
482 *Porous. Mater.* 8 (2001) 13-22.
- 483 [3] L. Lakiss, F. Ngoye, C. Can, S. Laforge, Y. Pouilloux, Z. Qin, M. Tarighi, K.
484 Thomas, V. Valtchev, A. Vicente, L. Pinard, J.-P. Gilson, C. Fernandez, J.
485 *Catal.* 328 (2015) 165-172.
- 486 [4] Z. Qin, L. Lakiss, L. Tosheva, J.-P. Gilson, A. Vicente, C. Fernandez,
487 V. Valtchev, *Adv. Funct. Mater.* 24 (2014) 257-264

- 488 [5] M. Guisnet, P. Magnoux, *Appl. Catal A: Gen.* 54 (1989) 1-27
- 489 [6] U. Olsbye, S. Svelle, M. Bjørgen, P. Beato, T.V.W. Janssens, F. Joensen, S.
490 Bordiga, K.P. Lillerud, *Angew. Chem. Int. Ed.* 51 (2012) 5810-5831.
- 491 [7] Z. Zhu, Q. Chen, Z. Xie, W. Yang, C. Li, *Microp. Mesopor. Mater.* 88 (2006)
492 16-21.
- 493 [8] L.-E. Sandoval-Díaz, J.-A. González-Amaya, C.-A. Trujillo, *Microp. Mesopor.*
494 *Mater.* 215 (2015) 229-243.
- 495 [9] A. Corma, *J. Catal.* 216 (2003) 298 – 312.
- 496 [10] Y. Gao, B. Zheng, G. Wu, F. Ma, C. Liu, *RSC Adv.* 6 (2016) 83581-83588.
- 497 [11] B. Bonelli, L. Forni, A. Aloise, J. B.Nagy, G. Fornasari, E. Garrone, A. Gedeon,
498 G. Giordano, F. Trifirò, *Microp. Mesop. Mater.* 101 (2007) 153-160.
- 499 [12] L. Forni, G. Fornasari, F. Trifirò, A. Aloise, A. Katovic, G. Giordane, J. B.Nagy,
500 *Microp. Mesop. Mater.* 101 (2007) 161-168.
- 501 [13] B. Wichterlová, N. Žilkova, E. Uvarova, J. Čejka, P. Sarv, C. Paganini, J.A.
502 Lercher, *Appl. Catal. A: Gen.* 182 (1999) 297-308.
- 503 [14] D. Chen, K. Moljord, T. Fuglerud, A. Holmen, *Microp. Mesopor. Mater.* 29
504 (1999) 191-203.
- 505 [15] F. Di Renzo, *Catal. Today* 41 (1998) 37-40.
- 506 [16] H. Konno, T. Okamura, T. Kawahara, Y. Nakasaka, T. Tago, T. Masuda, *Chem.*
507 *Eng. J.* 207 (2012) 490-496.
- 508 [17] S. Mintova, J.-P. Gilson, V. Valtchev, *Nanoscale* 5 (2013) 6693-6703.

- 509 [18] J. Pérez-Ramírez, C.H. Christensen, K. Egeblad, C.H. Christensen, J.C. Groen,
510 Chem. Soc. Rev. 37 (2008) 2530-2542.
- 511 [19] X. Chen, D. Xi, Q. Sun, N. Wang, Z. Dai, D. Fan, V. Valtchev, Microp. Mesop.
512 Mater. 234 (2016) 401-408.
- 513 [20] V. Valtchev, G. Majano, S. Mintova, J. Pérez-Ramírez, Chem. Soc. Rev. 42
514 (2013) 263-290.
- 515 [21] B. Bonelli, L. Forni, A. Aloise, J. B.Nagy, G. Fornasari, E. Garrone, A. Gadeon,
516 G. Giordano, F. Trifirò, Microp. Mesop. Mater. 101 (2007) 153-160.
- 517 [22] P. De Luca, D. Violante, D. Vuono, L. Catanzaro, J. B.Nagy, A. Nastro, Microp.
518 Mesop. Mater. 71 (2004) 39-49.
- 519 [23] N. Bilba, C.C. Pavel, I. Asaftei, A. Nastro, J. B.Nagy, C. Perry, D. Vuono, P. De
520 Luca, G. Iofsea, Stud. Surf. Sci. Catal. 154 (2004) 334-341.
- 521 [24] S. F. Abdo, S. T. Wilson, in: J. Cêjka, R. Morris, P. Nachtigall (Eds.), Zeolites
522 in catalysis: properties and applications, The Royal Society of Chemistry,
523 London, UK, 2017, RSC Catalysis Series 28, pp. 310-350.
- 524 [25] X. Chen, T. Todorova, A. Vimont, V. Ruaux, Z. Qin, J.-P. Gilson, V. Valtchev,
525 Microp. Mesop. Mater. 200 (2014) 334-342.
- 526 [26] Y. Kamimura, C. Kowenje, K. Yamanaka, K. Itabashi, A. Endo, T. Okubo,
527 Microp. Mesop. Mater. 181 (2013) 154-159.
- 528 [27] T.A. Semelsberger, R.L. Borup, H.L. Greene, J. Power Sources 156 (2006) 497
529 – 511.
- 530 [28] S.H. Park, C. S. Lee, Energ. Convers. Manage. 89 (2014) 848 – 863.

- 531 [29] T.H. Fleisch, A.Basu, R.A. Sills, *J. Nat. Gas Sci. Eng.* 9 (2012) 94 – 107.
- 532 [30] B.L. Salvi, K.A. Subramanian, N.L. Panwar, *Renew. Sust. Energ. Rev.* 25
533 (2013) 404 – 419.
- 534 [31] Z. Azizi, M. Rezaeimanesh, T. Tohidian, M. R. Rahimpour, *Chem. Eng.*
535 *Process.* 82 (2014) 150 – 172.
- 536 [32] P. Haro, F. Trippe, R. Stahl, E. Henrich, *Appl. Energ.* 108 (2013) 54-65.
- 537 [33] D. Chen, K. Moljord, A. Holmen, *Microp. Mesop. Mater.* 164 (2012) 239-250.
- 538 [34] E. Catizzone, G. Bonura, M. Migliori, F. Frusteri, G. Giordano, *Molecules*, 23
539 (2018) 31-58.
- 540 [35] M. Xu, J. H. Lunsford, D. W. Goodman, A. Bhattacharyya, *Appl. Catal. A: Gen.*
541 149 (1997) 289-301.
- 542 [36] S. P. Naik, T. Ryu, V. Bui, J. D. Miller, N. B. Drinnan, W. Zmierzak, *Chem.*
543 *Eng. J.* 167 (2011) 362 – 368.
- 544 [37] J. Ereña, R. Garoña, J. M. Arandes, A. T. Aguayo, J. Bilbao, *Int. J. Chem. React.*
545 *Eng.* 3 (2005).
- 546 [38] M. De Falco, M. Capocelli, G. Centi, *Chem. Eng. J.* 294 (2016) 400-409
- 547 [39] E. Catizzone, A. Aloise, M. Migliori, G. Giordano, *Microp. Mesop. Mater.* 243
548 (2017) 102-111.
- 549 [40] E. Catizzone, M. Milgiori, A. Purita, G. Giordano, *J. Energ. Chem.* 30 (2019)
550 162-169
- 551 [41] E. Catizzone, Z. Cirelli, A. Aloise, P. Lanzafame, M. Migliori, G. Giordano,
552 *Catal. Today* 304 (2018) 39-50.

- 553 [42] E. Catizzone, S. Van Daele, M. Bianco, A. Di Michele, A. Aloise, M. Migliori,
554 V. Valtchev, G. Giordano, *Appl. Catal. B: Env.* 243 (2019) 273-282.
- 555 [43] M. Migliori, E. Catizzone, A. Aloise, G. Bonura, L. Gómez-Hortigüela, L.
556 Frusteri, C. Cannilla, F. Frusteri, G. Giordano, *J. Ind. Eng. Chem.* 68 (2018)
557 196-208.
- 558 [44] G. Bonura, M. Migliori, L. Frusteri, C. Cannilla, E. Catizzone, G. Giordano, F.
559 Frusteri, *J. CO₂ Util.* 24 (2018) 398-406.
- 560 [45] F. Frusteri, G. Bonura, C. Cannilla, G. Drago Ferrante, A. Aloise, E. Catizzone,
561 M. Migliori, G. Giordano, *Appl. Catal. B: Env.* 176 (2015) 522-531.
- 562 [46] G. Bonura, F. Frusteri, C. Cannilla, G. Drago Ferrante, A. Aloise, E. Catizzone,
563 M. Migliori, G. Giordano, *Catal. Today* 277 (2016) 48-54.
- 564 [47] G. Bonura, C. Cannilla, L. Frusteri, A. Mezzapica, F. Frusteri, *Catal. Today* 281
565 (2017) 337-334.
- 566 [48] S.-H. Kang, J. W. Bae, K.-W. Jun, H. S. Potdar, *Catal. Comm.* 9 (2008) 2035-
567 2039.
- 568 [49] J. W. Jung, Y. J. Lee, S. H. Um, P. J. Yoo, D. H. Lee, K.-W. Jun, J. W. Bae,
569 *Appl. Catal. B: Env.* 126 (2012) 1-8.
- 570 [50] J. W. Bae, S.-H. Kang, Y.-J. Lee, K.-W. Jun, *Appl. Catal. B: Env.* 90 (2009)
571 426-435.
- 572 [51] J. H. Flores, D. P. B. Peixoto, L. G. Appel, R. R. de Avillez, M. I. Pais da Silva,
573 *Catal. Today* 172 (2011) 218-225.
- 574 [52] Q. Xe, P. Chen, P. Peng, S. Liu, P. Peng, B. Zhang, Y. Cheng, Y. Wan, Y. Liu,
575 R. Ruan, *RSC Adv.* 5 (2015) 26301-26307.

- 576 [53] P. S. S. Prasad, J. W. Bae, S.-H. Kang, Y.-J. Lee, K.-W. Jun, *Fuel Process.*
577 *Technol.* 89 (2008) 1281-1286.
- 578 [54] R. Montesano, A. Narvaez, D. Chadwick, *Appl. Catal. A: Gen.* 482 (2014) 69-
579 77.
- 580 [55] G. Guo, Y. Sun, Y. Long, *Chem. Comm.* 19 (2000) 1893-1894
- 581 [56] M. Migliori, A. Aloise, G. Giordano, *Catal. Today* 227 (2014) 138-143.
- 582 [57] P. Lanzafame, G. Papanikolaou, S. Perathoner, G. Centi, M. Migliori, E.
583 Catizzone, G. Giordano, *Appl. Catal. A: Gen.* 580 (2019) 186-196.
- 584 [58] E. Catizzone, A. Aloise, M. Migliori, G. Giordano, *Appl. Catal. A: Gen.* 502
585 (2015) 215-220.
- 586 [59] R. K. Ahedi, A. N. Kotasthane, B. S. Rao, A. Manna, B. D. Kulkarni, *J. Coll.*
587 *Inter. Sci.* 236 (2001) 47-51.
- 588 [60] B. Qian, G. Guo, X. Wang, Y. Zeng, Y. Sun, Y. Long, *Phys. Chem. Chem.*
589 *Phys.* 3 (2001) 4164-4169.
- 590

591 **TABLES CAPTIONS**

592 **Table 1** Chemical composition, pore volume and surfaces characteristics of
593 synthesised FER-type materials.

594 **Table 2** Acidic properties of investigated catalysts.

595 **Table 3** Calculated binding energies and lengths for the investigated SDA-FER
596 systems from DFT simulation

597

598

599 FIGURES CAPTIONS

- 600 **Figure 1** XRD pattern of FER samples synthesized with the following templates:
601 (A) ethylenediamine, (*) indicates the presence of Kaetite phase; (B)
602 pyrrolidine; (C) tetrahydrofuran, (▼) and (◆) denote the presence of
603 MOR and MFI phase, respectively; (D) 1,8-diaminooctane (DAO).
- 604 **Figure 2** SEM micrographs of FER-type materials synthesised with En (A), Py
605 (B), THF (C) and DAO (D).
- 606 **Figure 3** SEM (left) and TEM (right) micrographs of FER-type materials
607 synthesised by adding SLS to a Py-containing system.
- 608 **Figure 4** ^{27}Al MAS NMR spectra of the H-forms of ferrierite synthesized with En
609 (a), Py (b), THF (c) and DAO (d).
- 610 **Figure 5** NH_3 -TPD profiles of En-FER (a), Py-FER (b), THF-FER (c) and DAO-
611 FER (d).
- 612 **Figure 6** FT-IR spectra of OH groups of En-FER (a), Py-FER (b), THF-FER (c)
613 and DAO-FER (d) after evacuation at 300 °C for 4h.
- 614 **Figure 7** Fraction of Brønsted (●) and Lewis (■) acid sites free of adsorbed D_3CN
615 molecules as a function of desorption temperature; En-FER (A), Py-
616 FER(B), THF-FER(C) and DAO-FER(D).
- 617 **Figure 8** Methanol conversion as a function of reaction temperature over the
618 investigated samples; $\text{WHSV} = 4.5 \text{ h}^{-1}$.
- 619 **Figure 9** DME selectivity as a function of reaction temperature over the
620 investigated samples; $\text{WHSV} = 4.5 \text{ h}^{-1}$.
- 621 **Figure 10** Methanol conversion versus Time on Stream observed at 240 °C and
622 $\text{WHSV} = 4.5 \text{ h}^{-1}$.

623 **Figure 11** Carbon deposit over the investigated sample after 1000 min of TOS at
624 240 °C and WHSV= 4.5 h⁻¹.
625
626

<i>SAMPLE</i>	<i>Na/Al_{bulk}^a</i> <i>[mol/mol]</i>	<i>Si/Al_{bulk}^a</i> <i>[mol/mol]</i>	<i>S_{BET}^b</i> <i>[m²/g]</i>	<i>V_{mic}^c</i> <i>[cm³/g]</i>
Py-FER	0.1	8.4	329	0.131
En-FER	0.1	7.4	306	0.140
THF-FER	0.9	7.7	280	0.115
DAO-FER	0.6	6.6	287	0.125
SLS-Py-FER	0.1	8.4	340	0.133

^a Atomic absorption

^b BET superficial area

^c Micropore volume calculated by *t*-plot method

Table 1

<i>SAMPLE</i>	<i>NH₃-uptake</i> [$\mu\text{mol/g}_{\text{cat}}$]	<i>T_{M,LT}</i> ^a [°C]	<i>x_{LT}</i> ^[b]	<i>T_{M,HT}</i> ^c [°C]	<i>x_{HT}</i> ^d	<i>Lewis acid sites</i> ^e [%]	<i>Strong Lewis acid sites</i> ^f [%]
Py-FER	965	232	0.35	454	0.65	0.34	0.14
En-FER	1052	245	0.30	436	0.70	0.41	0.16
THF-FER	929	236	0.31	474	0.69	0.15	0.10
DAO-FER	1418	231	0.40	455	0.60	0.40	0.24
SLS-Py-FER	965	235	0.33	458	0.67	0.32	0.13

^a Temperature of maximum desorption of NH₃ between 100 and 300°C

^b Fractional population of sites between 100 and 300°C

^c Temperature of maximum desorption of NH₃ above 300°C

^d Fractional population of sites above 300°C

^e Estimated by FT-IR analysis of adsorbed D₃-acetonitrile at 25°C

^f Estimated by FT-IR analysis of adsorbed D₃-acetonitrile at 300°C

Table 2

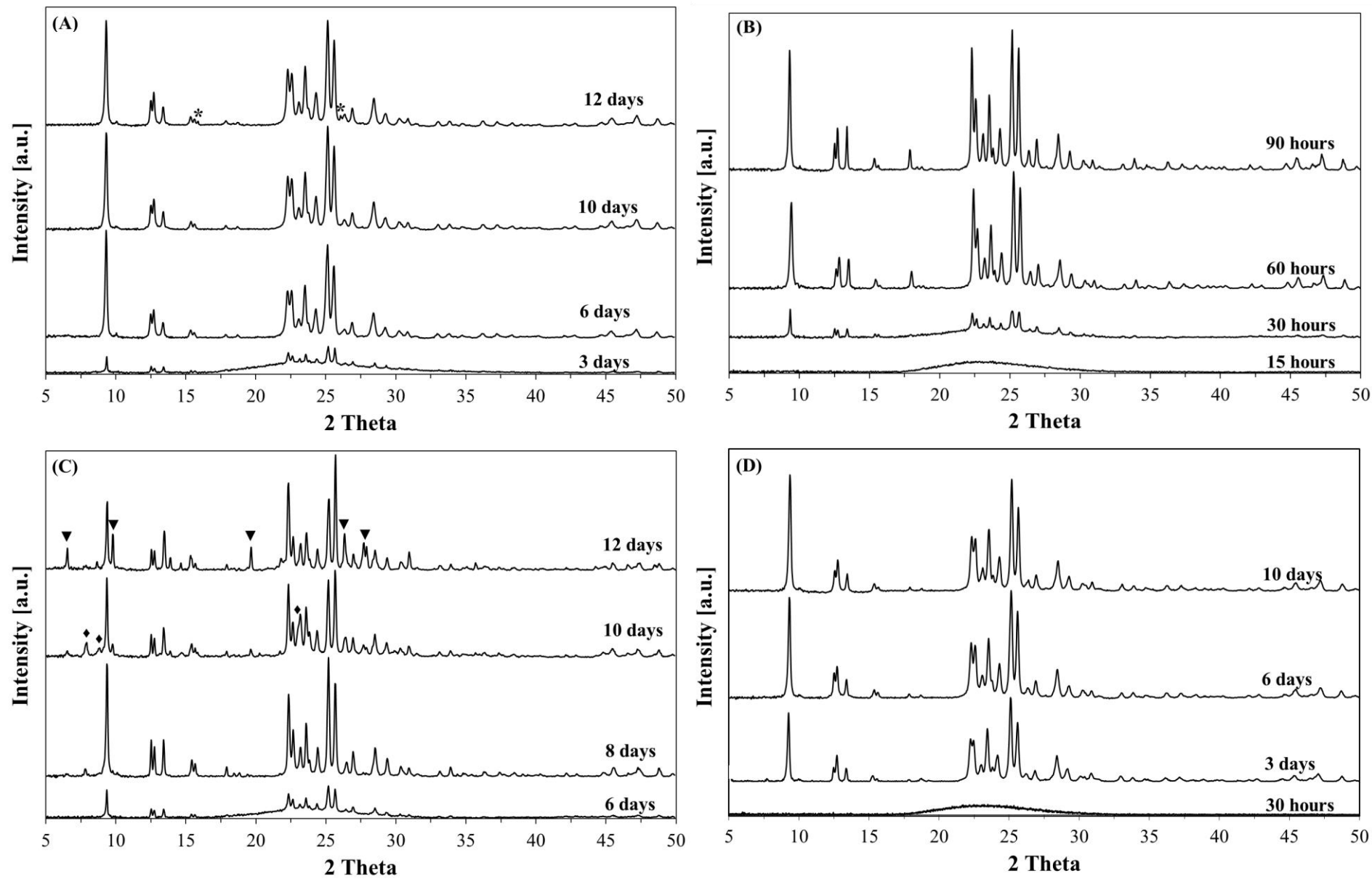


Figure 1

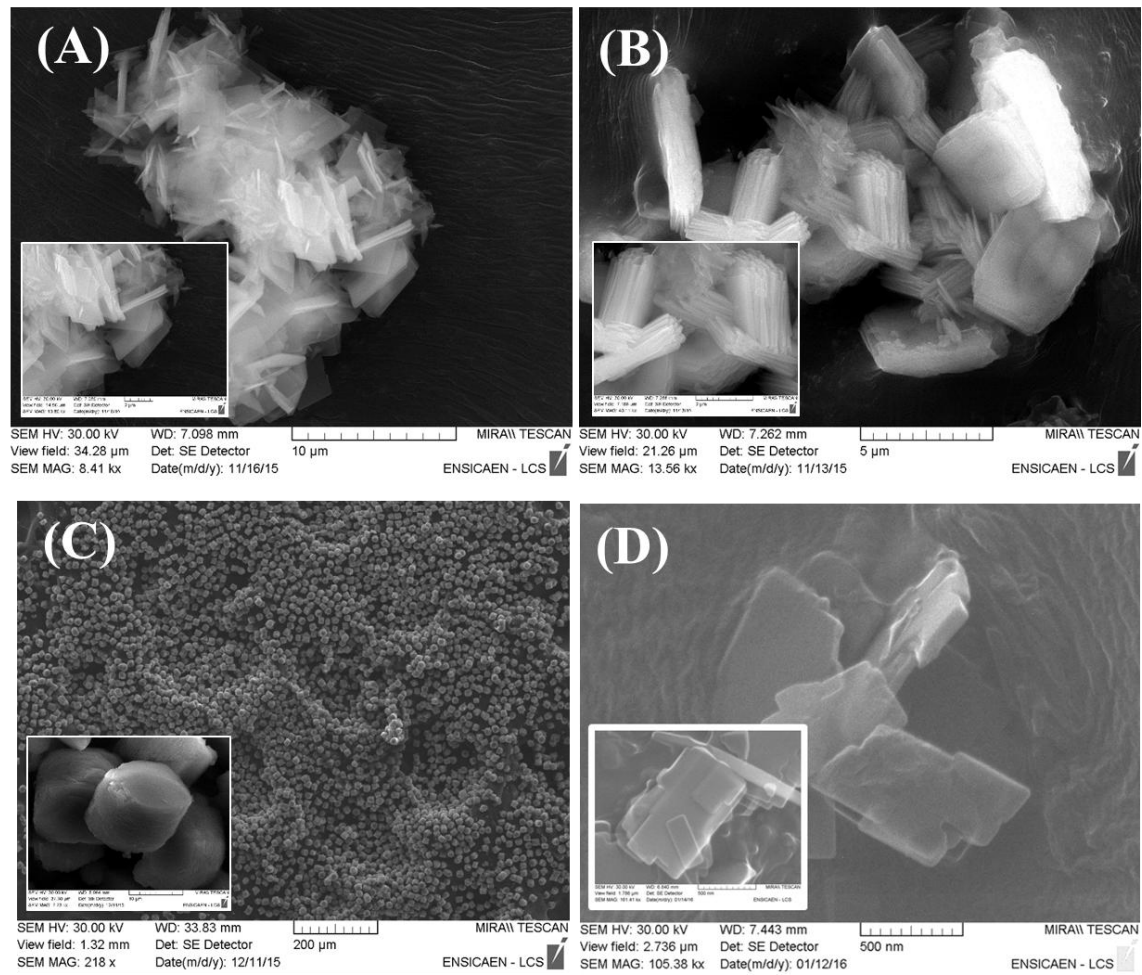


Figure 2

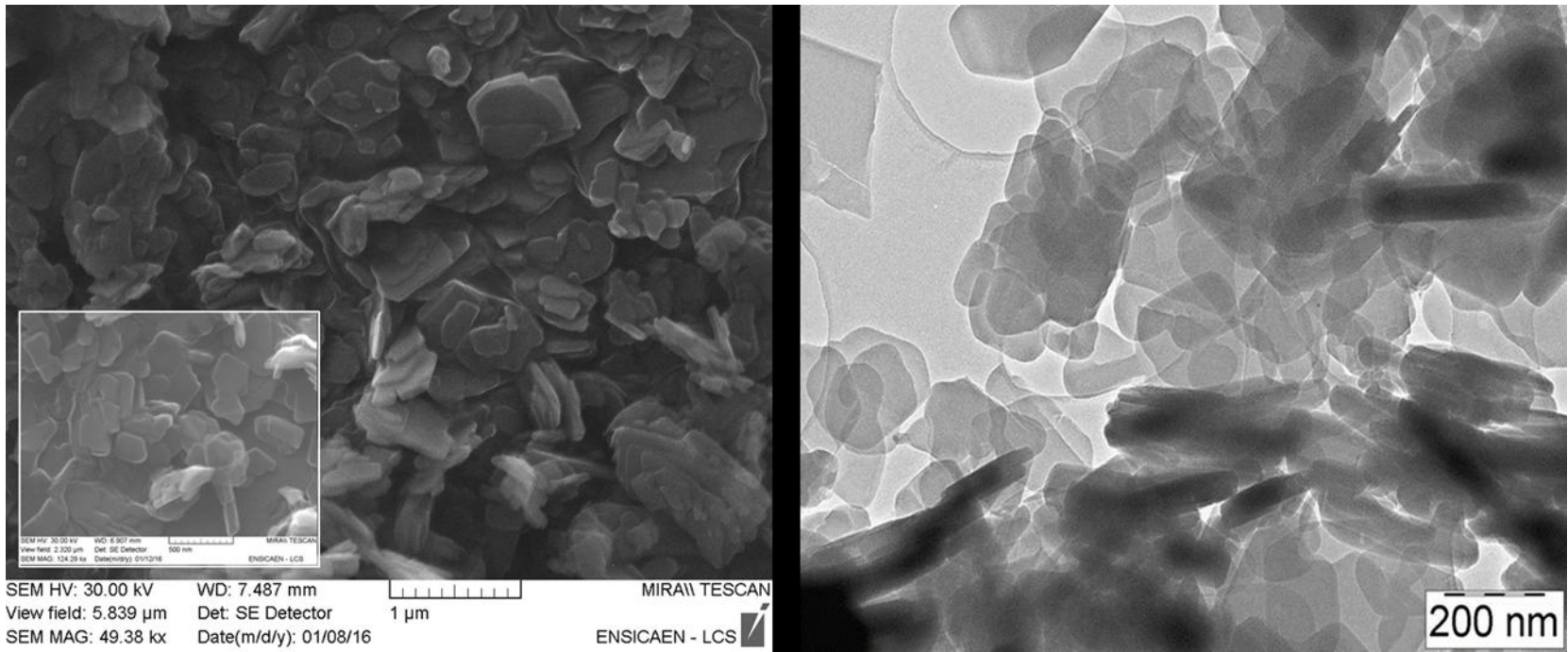


Figure 3

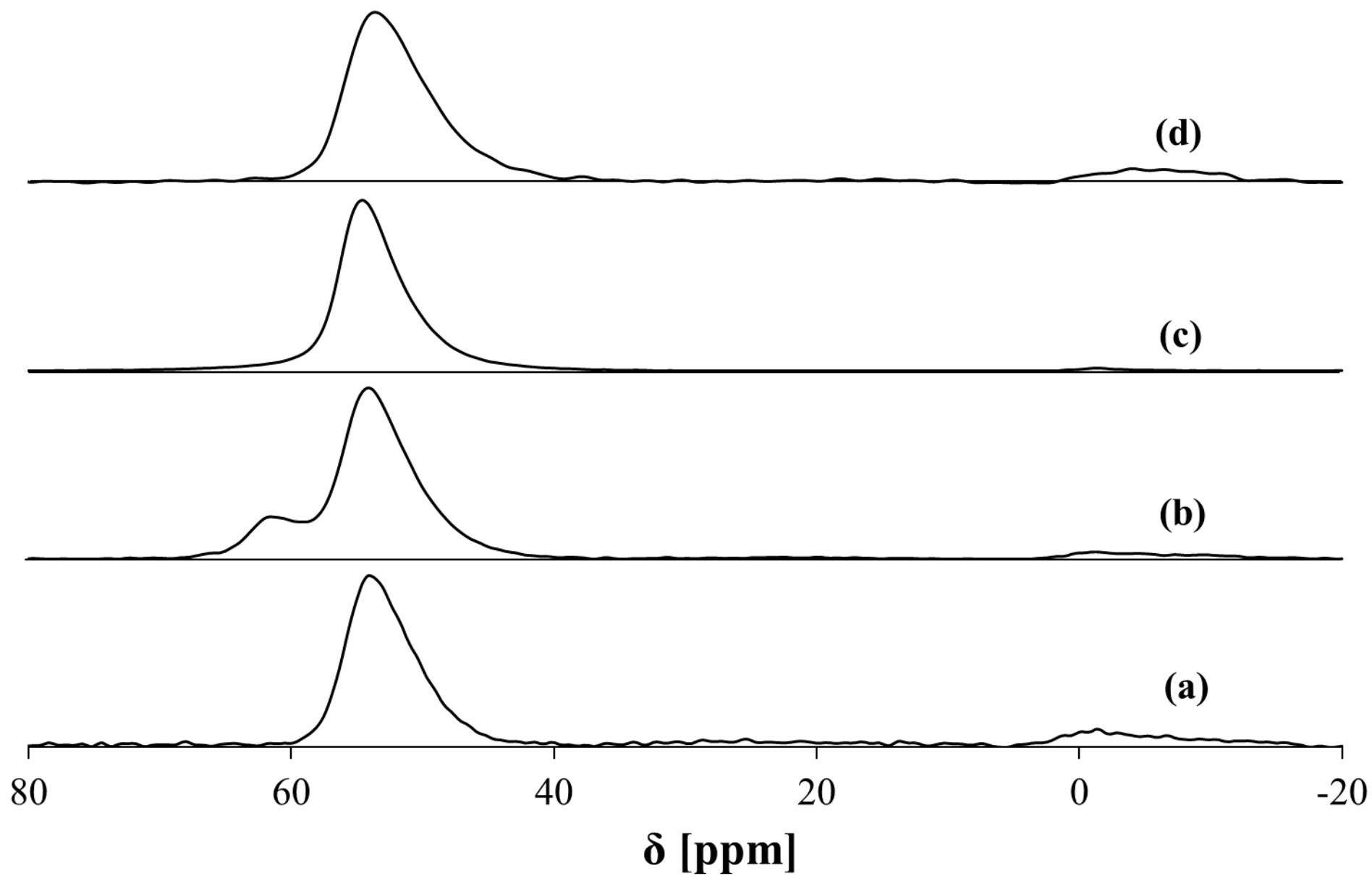


Figure 4

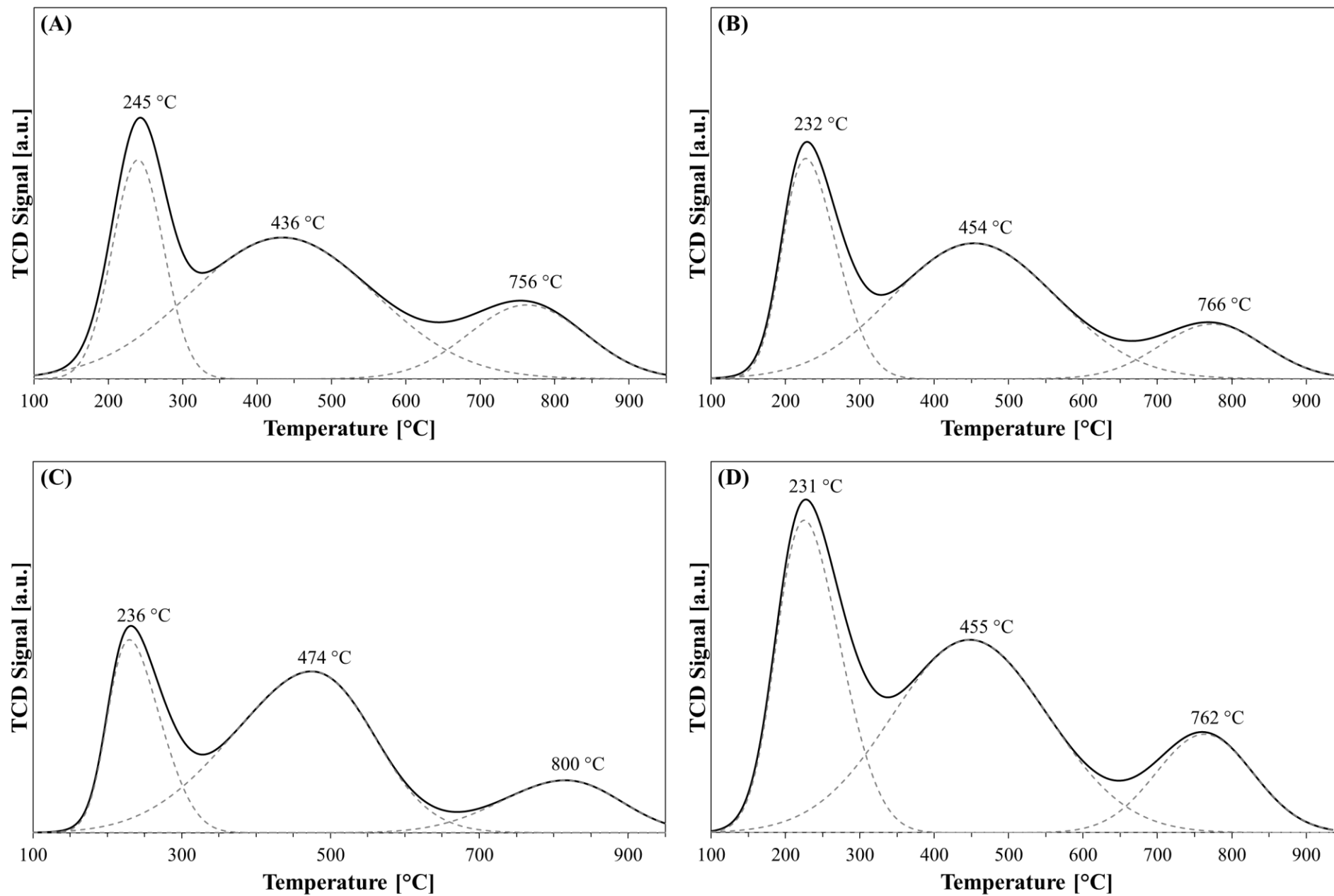


Figure 5

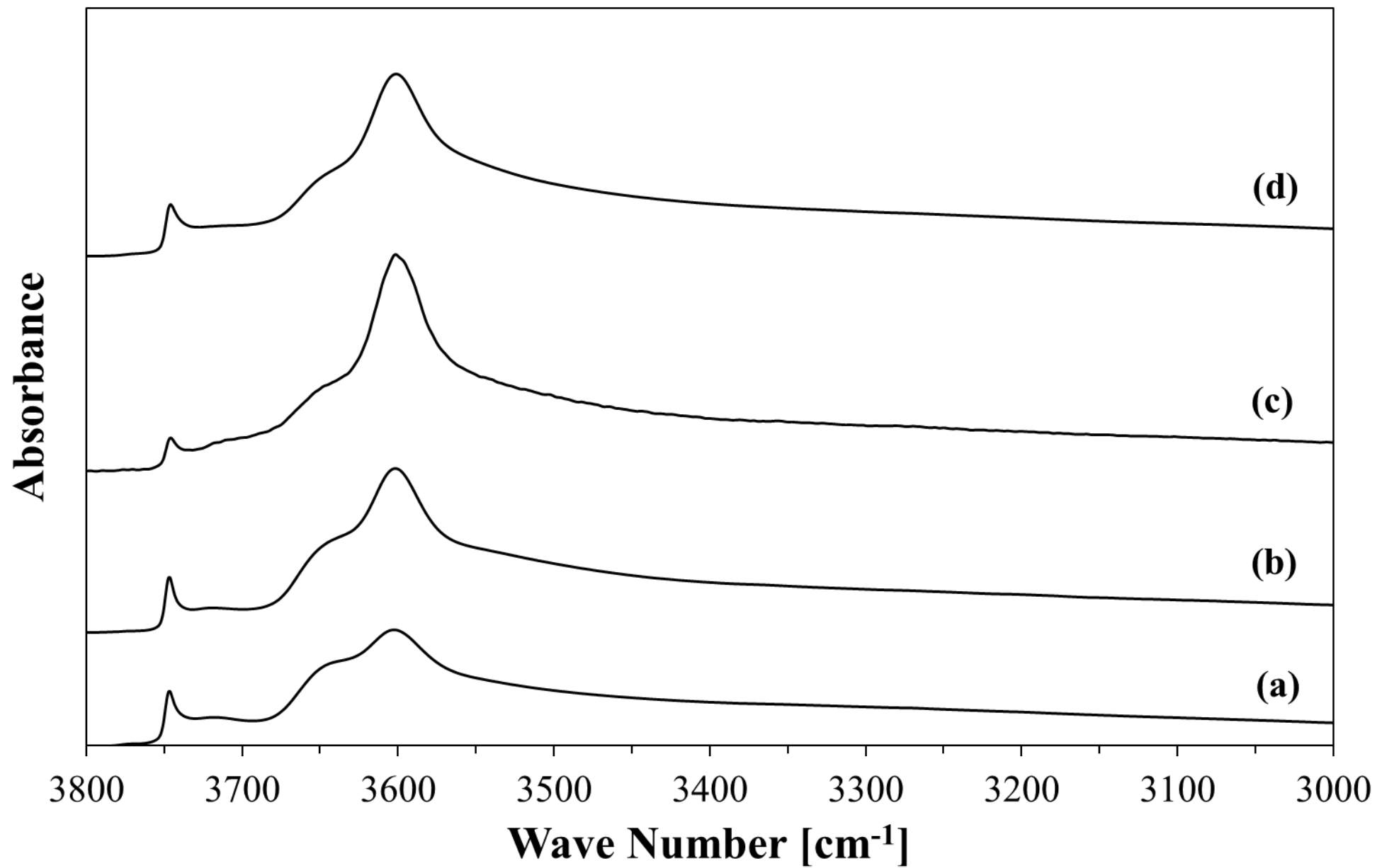


Figure 6

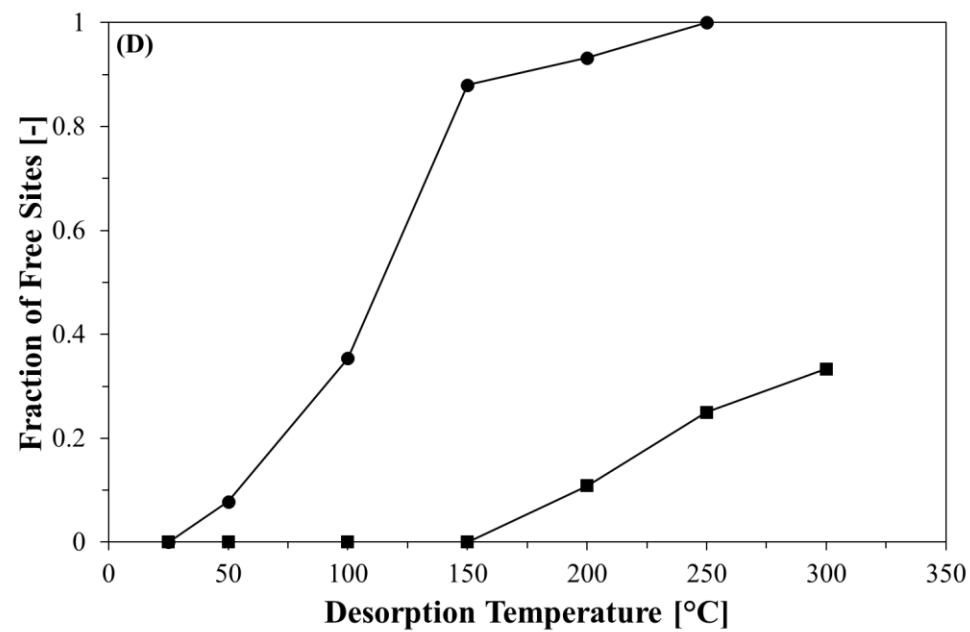
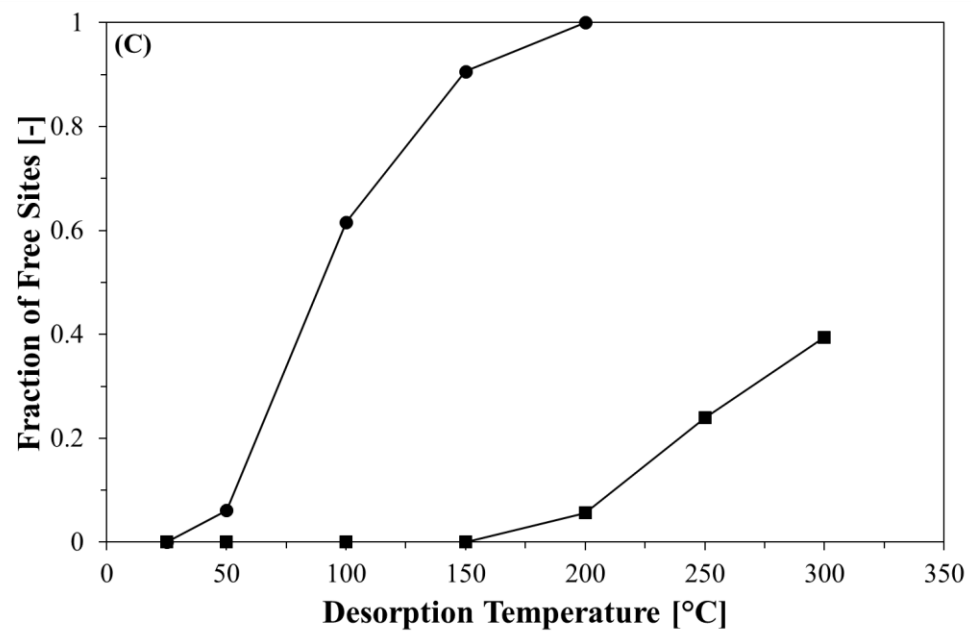
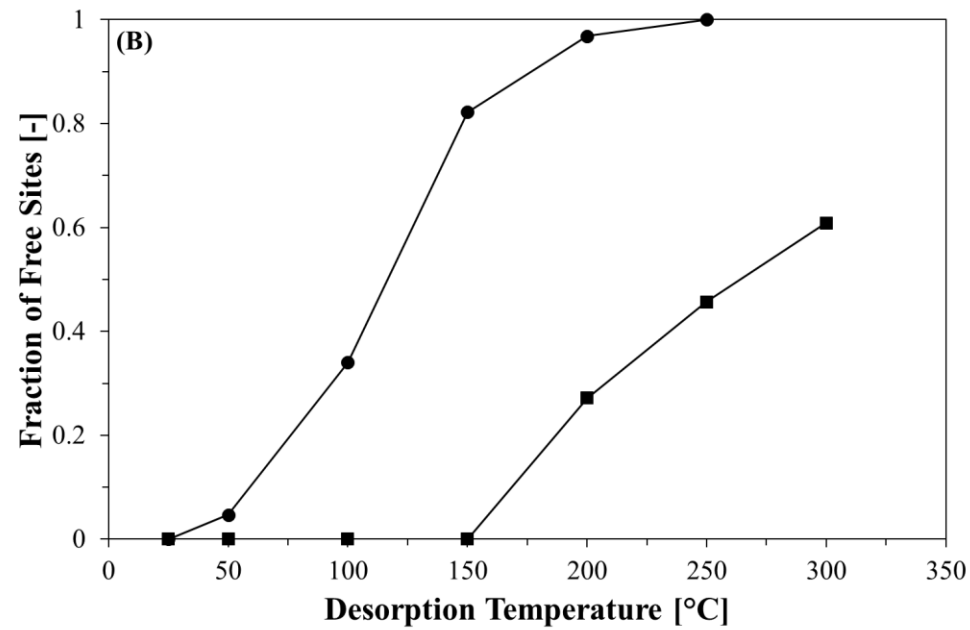
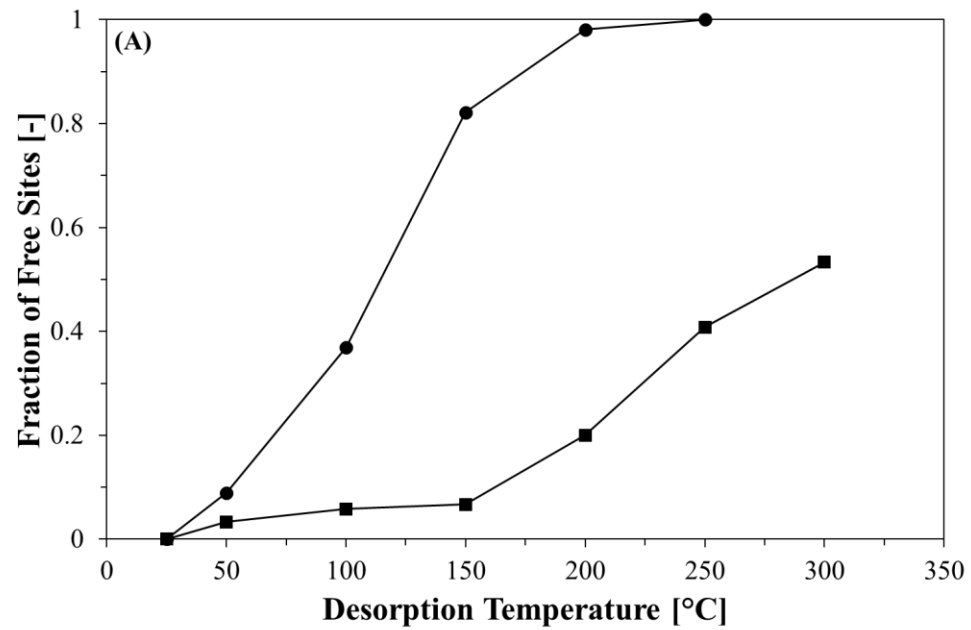


Figure 7

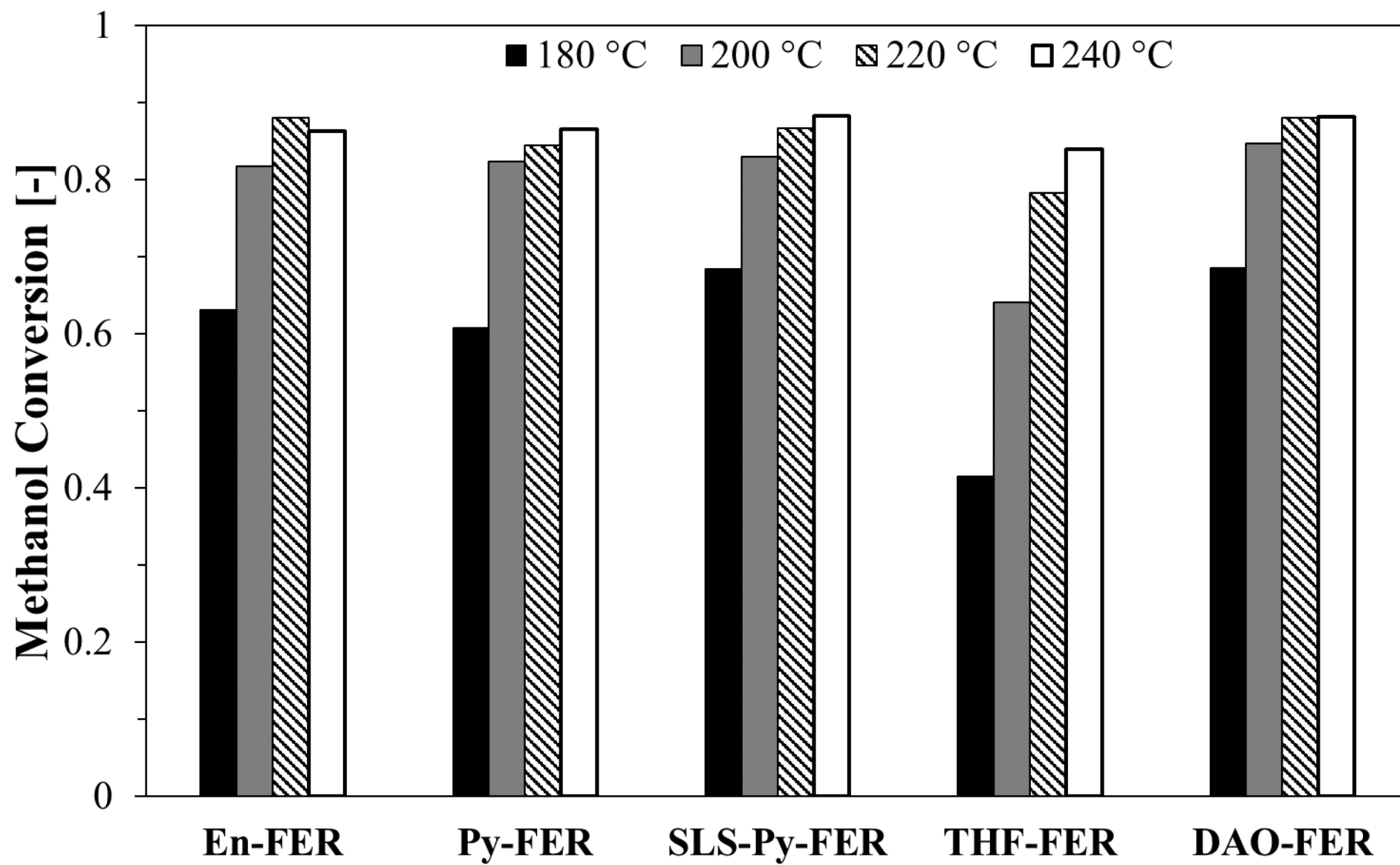


Figure 8

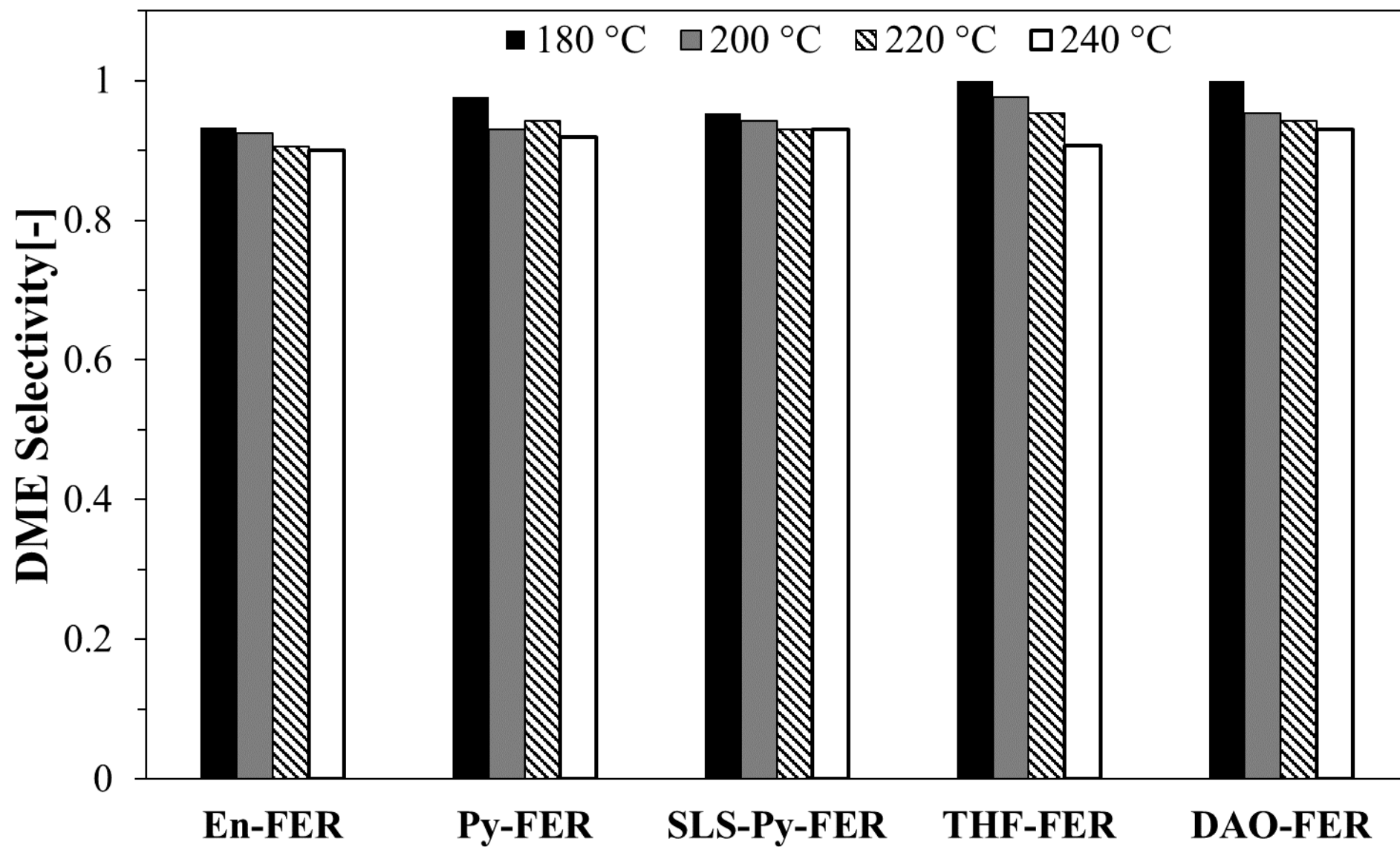


Figure 9

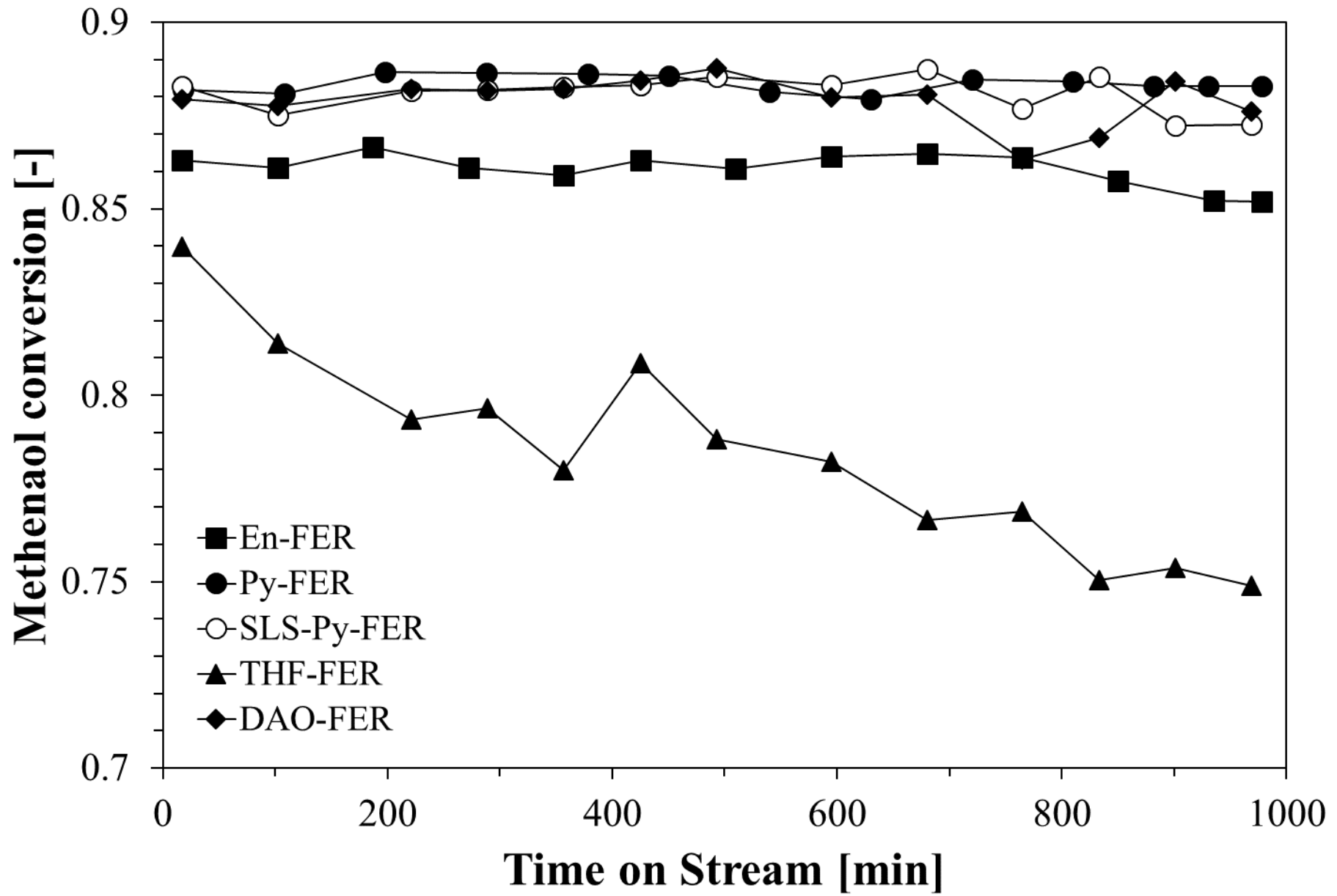


Figure 10

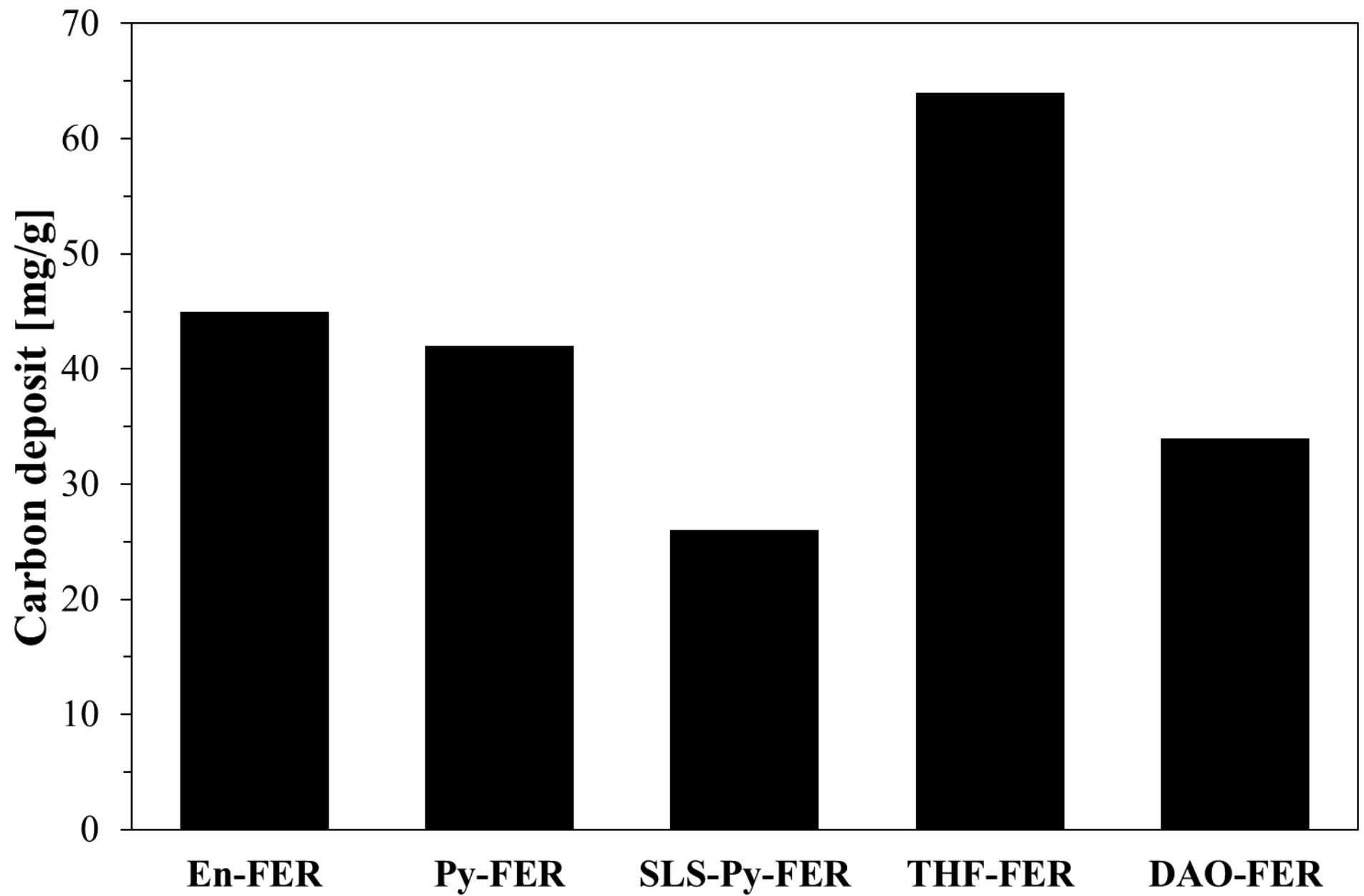


Figure 11